ADVANCED INTELLIGENT SYSTEMS
Open Access
www.advintellsyst.com

A Dual-Ion Multiphysics Model for Smart and Sustainable Sensors Based on Bacterial Cellulose

Francesca Sapuppo, Giovanna Di Pasquale, Salvatore Graziani, Sara Sadat Hosseini, Luca Patané, Antonino Pollicino, Carlo Trigona, and Maria Gabriella Xibilia*

Bacterial cellulose (BC) is an emerging smart material, synthesized through microbial fermentation of environmentally friendly substrates, including organic waste. When functionalized with ionic liquids (ILs) and coated with conductive polymers, BC forms soft, sustainable, and electroactive composites, making it suitable for sensors in soft robotics, wearable, biomedical, and environmental monitoring applications. However, modeling frameworks for BC–IL sensors are still lacking, hindering their integration into real-world applications. To bridge this gap and support smart material design, we propose a novel first-principle white-box modeling framework is proposed that couples a 2D finite element method (FEM) for mechanical deformation with 1D FEM sub-models for ion transport and voltage generation. Specifically, this work introduces the first dual-carrier multiphysics model for mechanoelectric transduction in BC–IL sensors. The model, experimentally calibrated and validated, resolves the spatio-temporal dynamics of mechanical deformation and dual-ion transport, including diffusion, electromigration, and advection. By explicitly incorporating the transport and interaction of both cations and anions, previously neglected in smart-sensors modeling, the proposed strategy provides a foundational simulation framework for the scalable, rapid, and intelligent design of next-generation biodegradable and multifunctional smart sensors, advancing the integration of green materials into intelligent systems.

1. Introduction

Electroactive polymers (EAPs) have attracted growing interest in industrial applications due to their potential to enable flexible, lightweight, and tunable electromechanical devices.[1] Their ability to convert electrical energy into mechanical motion (electromechanical transduction) and mechanical deformation into electrical signals (mechanoelectrical transduction) makes them suitable for applications ranging from biomedical devices and soft robotics to aerospace and consumer electronics.[2–5]

In this context, recent advances in soft robotics underscore the increasing role of intelligent polymer-based actuators in multifunctional applications such as drug delivery, wearable systems, and biomimetic motion, as reviewed in ref. [6,7] These materials provide unique opportunities for developing compliant and programmable robotic systems, with ionic polymer–metal composites (IPMCs) standing out as promising electrically driven actuators due to their rapid response and mechanical robustness.[4]

Among EAPs, ionic EAPs (IEAPs), such as IPMCs and carbon-polymer composites, have been extensively studied due to their large deformation under low voltage and bioinspired actuation capabilities. While actuation electromechanical transduction in IEAPs has been extensively characterized[4,6,8–11] in terms of mass transport principles and actuation mechanism, the inverse mechanoelectrical transduction process in IEAP-based sensors remains comparatively underexplored, despite promising applications in biomedical sensing,[12–14] vibration energy harvesting, and self-powered sensing.[15] This research gap is particularly relevant in the context of soft sensing transductors development, where dynamic ion redistribution under mechanical deformation offers a rich mechanism for signal generation but lacks comprehensive multiphysics modeling frameworks. In parallel with the functional advances of EAPs, the electronics industry is

F. Sapuppo, L. Patané, M. G. Xibilia
Department of Engineering
University of Messina
98158 Messina, Italy
E-mail: francesca.sapuppo@unime.it

The ORCID identification number(s) for the author(s) of this article can be found under https://doi.org/10.1002/aisy.202500579.

DOI: 10.1002/aisy.202500579

G. Di Pasquale
Department of Chemical Science
University of Catania
95125 Catania, Italy

S. Graziani, S. S. Hosseini, C. Trigona
Department of Electrical Electronics and Information Engineering
University of Catania
95125 Catania, Italy

A. Pollicino
Department of Civil Engineering and Architecture
University of Catania
95125 Catania, Italy

undergoing a transformation toward environmentally sustainable materials and processes. This shift has led to the emergence of green electronics, in which biodegradable and bio-derived materials play a central role.

Bacterial cellulose (BC), produced by strains such as *Acetobacter xylinum* and *Gluconacetobacter hansenii*, is a leading candidate due to its renewable origin, high purity, and porous structure suitable for functionalization with ionic liquids (ILs). Although chemically identical to plant-derived cellulose, BC is produced via microbial fermentation using green feeding media (e.g., banana peel[16]) in standard laboratory environments. Unlike plant-based cellulose, its production avoids deforestation, yields a highly pure material, and results in a fully biodegradable substrate suitable for flexible, printable, and biocompatible electronic devices.[17] Its mechanical resilience and environmental compatibility enable use in soft robotics, wearable electronics, smart packaging, and biomedical systems.[18]

When BC is functionalized with ILs and coated with conductive polymers, it becomes electroactive and is suitable for use in both actuators and sensors.[19–21] These BC–IL-based composites can therefore be classified as IEAPs, offering a sustainable alternative to synthetic polymers by combining functional performance with compatibility for roll-to-roll manufacturing processes.[21–24] Importantly, IL derived from biomolecules, so-called bio-ILs have been shown to improve biocompatibility, cytocompatibility, and environmental safety, thereby expanding the use of BC-based IEAPs in biomedical applications such as implantable sensors and smart drug-delivery devices.[25] These bioinspired systems are at the forefront of smart tissue engineering, molecular diagnostics, and regenerative medical electronics.

In particular, the dual functionality of BC-based transducers, as both sensors and actuators, has opened new possibilities for soft robotic systems that require both adaptability and environmental integration. Recent reviews highlight the role of electroactive biomaterials like BC–IL composites in responsive biointerfaces and distributed robotic actuation.[5] These materials support deformation-based sensing and controlled mechanical motion within the same lightweight and flexible platform.

Despite this potential, the design and optimization of BC-based IEAP sensors face significant challenges. On the one hand, EAP modeling frameworks, including black-box and gray-box and machine learning approaches,[4,15,26–29] rely on empirical data and lack physical insight and generalizability across different materials and operating conditions. On the other hand, first-principle models based on computational methods have proven effective for the simulation of multiphysical systems for different compound materials. These models are able to address a variety of physical domains, including carrier transport,[12,30] mechanical deformation,[31] thermal properties,[32] and magneto-mechanical interaction at the microscale.[33] However, their high computational cost often makes them impractical for fast design iterations, an essential requirement for industrial prototyping and real-time system optimization, thus highlighting the inherent trade-off between simulation accuracy and computational efficiency. Addressing this trade-off is central to enabling high-throughput simulation pipelines for material screening and rapid sensor optimization.

More specifically, in the IEAP modeling environment, white-box models based on first physics principles have been successfully developed for actuation purposes.[4,9,30,34,35] However, their application to mechanoelectric sensor technology remains very limited in the literature and is typically restricted to simplified single-ion transport models within solvent-based systems, primarily water-based electrolytes.[4,12,14,36] In the case of BC-based sensors, existing modeling efforts are still in a preliminary stage and primarily rely on gray-box approaches.[21,37]

To overcome these limitations and advance the development of multifunctional, intelligent, and eco-sustainable devices, this work introduces a novel first-principles modeling framework explicitly designed for BC-based ionic transducers, capturing the dual-carrier transport behavior characteristic of functionalized cellulose systems. The model captures the complexity of dual-ion electromechanical behavior, including diffusion, advection, and electromigration in porous substrates, while remaining computationally efficient through a hybrid dimensional approach. This lays the foundation for high-throughput simulation pipelines tailored to soft intelligent systems that integrate sensing, actuation, and adaptive responsiveness within a single sustainable platform, leveraging the demonstrated potential of BC composites in soft robotics and wearable bioelectronics.

To implement this, we integrate a 2D finite element method (FEM) for mechanical deformation with a series of 1D FEM formulations for ionic transport and electric potential generation. This dimensional decomposition is designed to preserve the fundamental physics of electromechanical coupling while reducing the computational effort. This facilitates fast parametric studies and supports the design and optimization of sensors at an early stage. The framework supports predictive material design, enabling the identification of structure–function relationships and critical design parameters, with direct validation through experimental measurements. Particular attention will be paid to ensuring that the model is compatible with data from real experimental setups to enable meaningful calibration and validation.

Ultimately, this methodology aims to provide a robust and scalable simulation framework for the design of next-generation green electronic devices based on BC–IL composites. To this end, the main contributions and novelties of this work include the introduction of a first-principles-based model specifically tailored for BC–IL sensors, establishing a bridge between sustainable smart sensors and high-fidelity multiphysics simulation. This study also presents the first dual-carrier FEM-based model for ionic EAPs, extending beyond traditional single-ion approximations typically employed in IL-functionalized soft transducers. Furthermore, it proposes a computationally efficient hybrid 2D–1D modeling strategy that supports fast-prototyping workflows for early-stage material design and parametric optimization, while laying the groundwork for high-throughput simulation pipelines.

The remainder of this article is structured as follows. Section 2 describes the fabrication and characterization of the BC-based sensor, including details on the materials used, geometry, and the experimental setup. Section 3 introduces the proposed dual-carrier multiphysics modeling framework, detailing the mechanical, chemical, and electrical subsystems and Section 4.1 their FEM implementation. Section 4.2 presents a comparative analysis between simulation results and experimental data,

including model calibration, spatial sensitivity evaluation, and ionic transport analysis. Finally, Section 5 outlines the key findings and implications of this modeling approach for the development of sustainable, intelligent sensor systems based on BC.

2. Experimental Section

2.1. Sensor Geometry and Manufacturing

The BC-based sensor is a composite material produced using the following materials: purified BC films (CBP-GS0010) purchased from BioFaber (Italy), approximately A4 size and average thickness t_{BC}; 1-Ethyl-3-Methylimidazolium tetrafluoroborate (EMIM-BF_4) purchased from Sigma Aldrich and used as IL, CLEVIOS PH 1000; an aqueous dispersion of poly(3,4-ethylenedioxythiophene)/polystyrene sulfonate (PEDOT:PSS), which was purchased from Heraeus and used for electrode fabrication. It should be noted that while BC is fully biodegradable and originates from renewable microbial fermentation, the IL EMIM-BF_4 and the conducting polymer PEDOT:PSS employed in this work are not currently classified as biodegradable. Nevertheless, EMIM-BF_4 was characterized by low volatility and reduced environmental impact compared to conventional organic solvents, and PEDOT:PSS is widely used in organic electronics because of its aqueous processability and stability. Our research explored BILs such as vitamin J-based derivative[38] and biodegradable conductive polymers[39] as possible alternatives. Therefore, the investigated device represented a step toward the realization of fully biodegradable self-generating motion sensors. The proposed multiphysics model provided a general modeling framework validated on a BC-based system, while future developments will focus on achieving sensor architectures composed entirely of biodegradable components.

The fabrication process began with BC, which was processed in squared samples measuring 5 cm × 5 cm. Each sample was immersed in EMIM-BF_4 for 24 h at room temperature in a laboratory desiccator using calcium chloride as the desiccant. After impregnation, excess IL was removed with filter paper. At this stage, the BC–IL composite contained ≈8% by weight of EMIM-BF_4. PEDOT/PSS electrodes were then deposited on both sides of the composite using a 25 µm film spreader. Finally, the transducers were trimmed to the desired geometry. No electrode lift-off was observed during trimming, handling, or under the cyclic bending used for characterization.

The geometry of the device is presented in **Figure 1**a, and its parameters are reported in **Table 1**, where L is the total length of

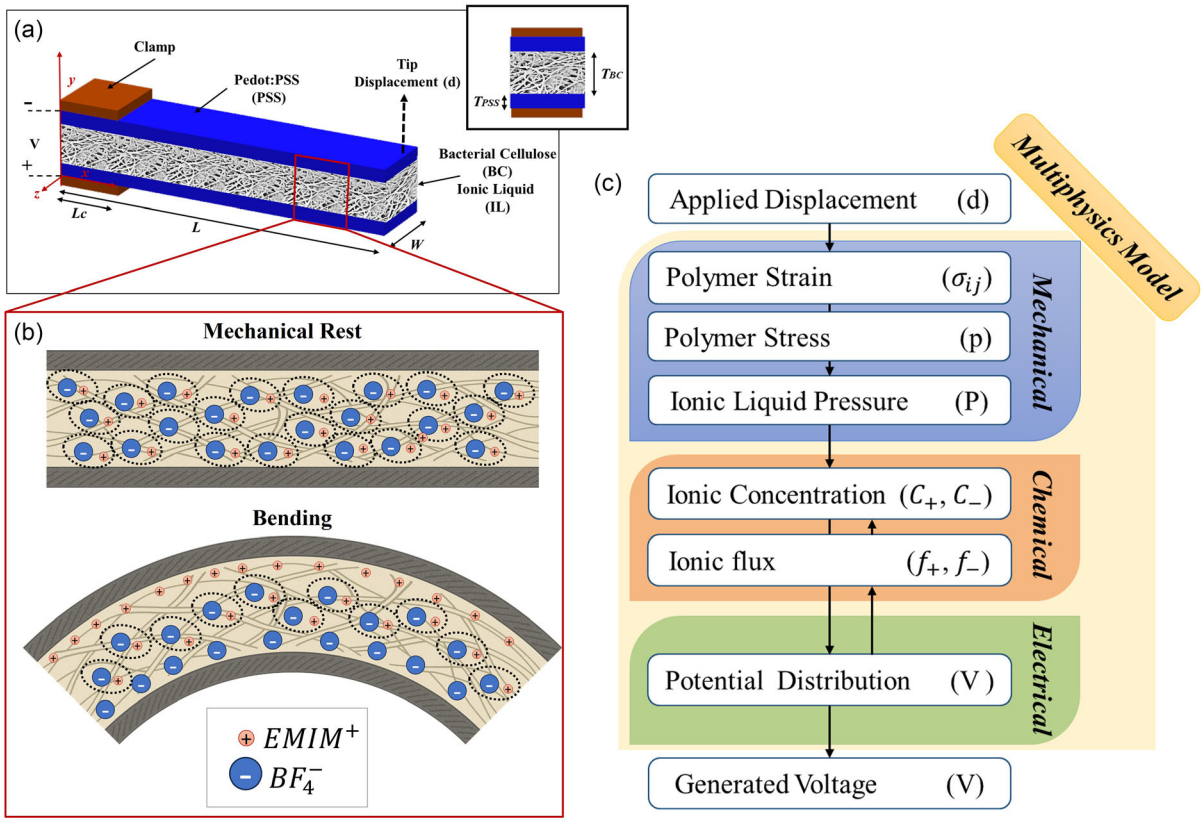

Figure 1. Multiphysics modeling framework for BC-based ionic sensors. a) Geometry of the BC-based sensor configured as a cantilever, with PEDOT:PSS electrodes applied to both sides of the IL-infused BC membrane and voltage measured in a OC configuration. Geometric parameters are reported in Table 1 and the complete setup in the Methods section. b) Schematic illustration of the dual-ion sensing mechanism showing the ionic distribution at rest and its redistribution under bending deformation. It highlights the role of both cations and anions in charge separation. c) Overview of the proposed multiphysics simulation framework, coupling mechanical deformation with ionic transport and voltage generation, used to compute the sensor electrical response to tip displacement.

Table 1. Geometrical parameters.

Parameter description	Value	Unit
Total length, L	4	cm
Total width, W	1	cm
Clamp region length, L_c	1.5	cm
Thickness of BC, T_{BC}	320	μm
Thickness of PEDOT, T_{PSS}	25	μm

the sample, W is the width of the entire sample, and L_c is the length of the clamped copper electrode. In particular, T_{BC} and T_{PSS} are the thicknesses of the BC and PEDOT/PSS electrodes, respectively. They were determined from scanning electron microscope (SEM) micrographs obtained using an EVO SEM (Zeiss, Cambridge, UK) instrument equipped with an energy dispersive X-ray spectrometry (EDX) microanalysis facility. The analyzes were performed by setting a high electron beam voltage of 20 kV and using a LaB6 (Lanthanum Hexaboride) emitter as the electron source. To perform the SEM analysis, the samples were coated with a thin gold film applied by a sputtering process using an Agar Sputter Coater AGB7340 spray coating machine (Assing, Italy).

2.2. Measurement Setup

The experimental configuration is illustrated in **Figure 2**: (a) CAD rendering of the mechanical system, (b) schematic of the complete experimental setup, and (c) photograph of the assembled device showing the cantilever-mounted sensor in its working configuration. A vertical threaded rod with two adjustable nuts was used to fine-tune the vertical positioning of the cantilever beam. A dedicated bracket attached to the

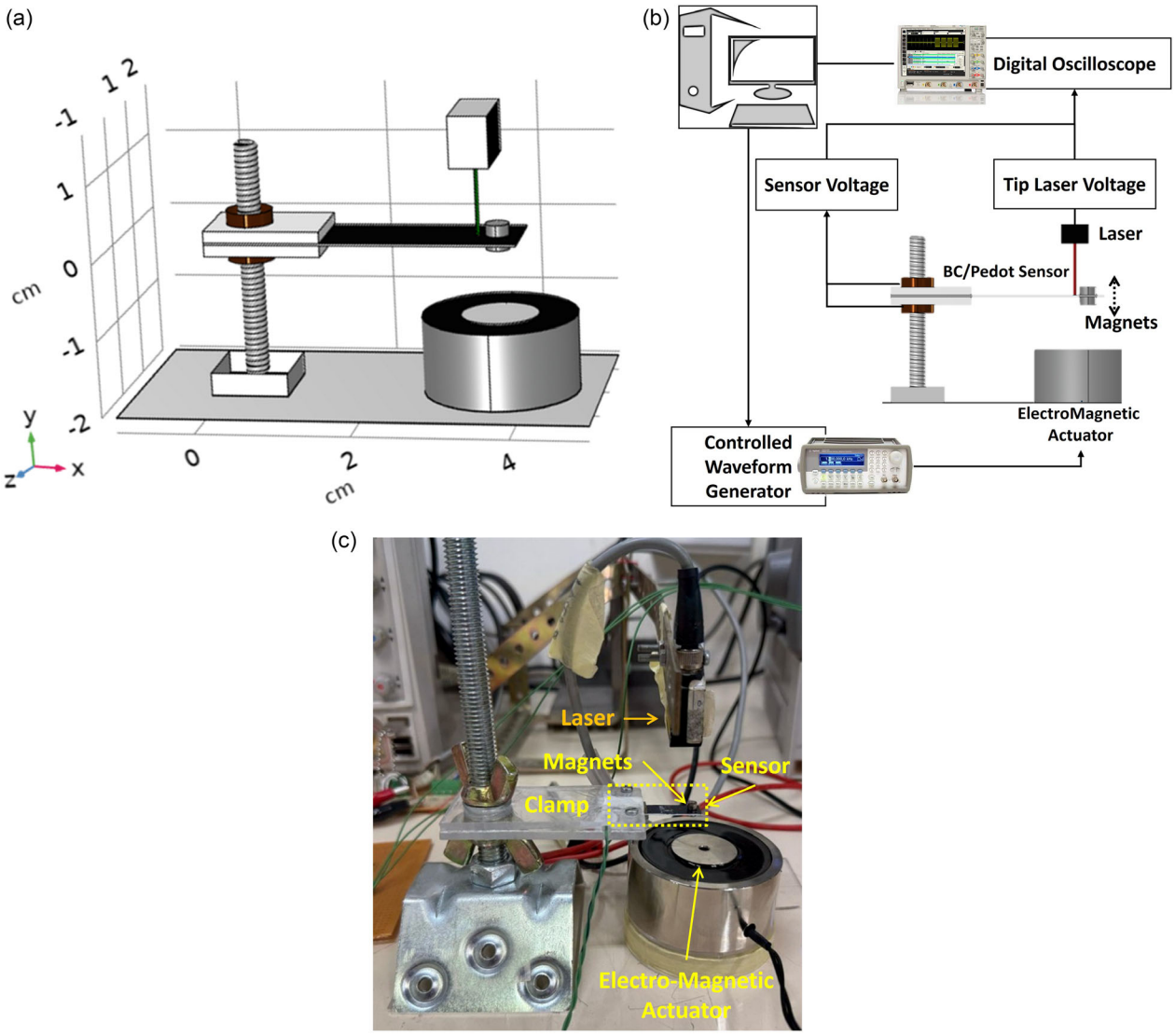

Figure 2. Mechanical setup: a) 3D schematic, b) global schematic of the acquisition system, c) laboratory setup.

threaded rod served as a support for the transducer. A custom rectangular housing was designed to accommodate a pair of rigid electrodes and the BC-based sensor. These electrodes were responsible for detecting the electrical signal generated by the composite material during deformation. To facilitate the connection between the electrodes and the external recording system, two conduit channels were integrated into the housing design. To ensure mechanical symmetry and proper housing, two identical brackets were fabricated and mounted opposite each other, enclosing the BC-based transducer and the pair of electrodes. The entire support structure was mounted on a base plate, which provided a stable foundation for the experimental setup. The mechanical excitation of the transducer was achieved with the help of an electromagnet located in a circular housing mounted on the base plate (see Figure 2a). The electromagnet used was the HS-P65*30 model from Heschen, with a diameter of 65 mm, a height of 30 mm, and a maximum DC voltage of 24 V. To drive the electromagnet, a power amplifier circuit was implemented with an OPA547 operational amplifier configured with two resistors of 4.7 and 6.8 kΩ. The actuation signal was synthesized in MATLAB®, then exported and loaded into a waveform generator (Keysight 33220A). The output signal from the waveform generator was fed into the power amplifier, which drives the electromagnet. This produces a motion of the tip of the BC sensor. The mechanical actuation was accomplished using two cylindrical magnets (mass: 0.32 g; radius: 2 mm; height: 3 mm) mounted symmetrically on both sides of the transducer near its free end at a distance $L_M = 3.7$ cm from the base clamp, commonly referred to as the beam tip. The displacement of the beam tip was monitored via a Baumer 12U6460-S35A laser displacement sensor with a resolution of ≈2 μm and adjustable sensitivity. The laser was focused at a distance of $L_L = 3.2$ cm from the base clamp. The mechanical deformation of the composite led to a charge accumulation on the PEDOT:PSS electrodes. This accumulation was measured as the open circuit (OC) voltage, hereafter referred to as sensor voltage. For the OC measurements, the electrodes were connected directly to an Agilent Infiniium MSO9064A digital oscilloscope. This simultaneously acquired the laser signal, allowing synchronous analysis of the mechanical input and electrical output. During experimental testing, the interface between PEDOT:PSS and BC–IL exhibited stable behavior, ensuring reproducible sensor responses.[40,41] These results indicated that the adopted fabrication route provided robust interfaces despite the aqueous solubility of the components.

3. Dual-Carrier Multiphysics Model

The BC-based transducer can convert mechanical deformation into an electrical signal and vice versa, and can act as both a sensor and an actuator. In this study, we investigated a BC-based sensor infused with EMIM-BF_4 as IL and coated with PEDOT:PSS as conductive polymers. This setup is illustrated in Figure 1a. When configured as a cantilever and used as a sensor, the mobile IL ions, $EMIM^+$ (cation) and BF_4^- (anion), redistribute within the BC matrix in response to an external force applied, inducing mechanical deformation (see Figure 1b). This ion redistribution leads to the generation of an electrical potential in the BC, which can be measured at the electrodes as open-circuit voltage, hereinafter denoted as the sensor output.

Multiphysics models for IEAPs have been explored in the literature.[12,34,36] These models typically couple three physical domains: a mechanical model to compute structural deformation, a chemical model to describe ionic transport, and an electrical model to calculate the internal voltage potential. The system behavior is generally governed by partial differential equations defined over the spatial domain $\boldsymbol{r} = (x, y, z)$ and time t. However, in the existing approaches, the chemical domain was limited to a single mobile ionic species, often assuming either cationic or anionic transport while treating the counterion as immobile or uniformly distributed. This simplification neglects the dynamics of both ionic carriers, which can be significant in systems based on ILs where both cations and anions are mobile and participate in the charge redistribution process (Figure 1b). Figure 1c presents the proposed multiphysics simulation framework, which couples mechanical deformation, ionic transport, and voltage generation through multiphysics integrating mechanical, chemical, and electrical models. Each of these sub-models is described in detail in the following section. The assumptions of isotropy, homogeneity, temporal invariance, and linearity are made for all materials.

3.1. Mechanical Model

Newton's second law relates the displacement ($\boldsymbol{d}$) to the volumetric force ($\boldsymbol{F}$), as reported in Equation (1).

$$\rho \frac{\partial^2 d(r,t)}{\partial t^2} - \nabla \cdot c \nabla d(r,t) = F(r,t) \tag{1}$$

where ρ is material density and c is the Navier constant.

The polymer pressure (p) is related to the σ_{ij} stress tensor components as in Equation (2)

$$p(r,t) = \frac{\sigma_{11} + \sigma_{22} + \sigma_{33}}{3} \tag{2}$$

Then, using the momentum conservation law in Equation (3), it is possible to relate the hydrostatic pressure p in the polymer with the fluid pressure (P)

$$\nabla P(r,t) = -\nabla p(r,t) \tag{3}$$

3.2. Chemical Model

A key novelty of this work lies in the chemical model, where both cations and anions are considered as mobile carriers, unlike conventional models that assume a single mobile species. Accordingly, distinct transport equations were formulated for each ionic species to capture their individual contributions to the total ionic current. The flux of cations $EMIM^+$ and of the anion BF_4^- was related to the time variation of their respective concentrations C_+ and C_-, the applied potential (V), and to the fluid pressure (P). It is calculated by the Nernst–Planck law as follows

$$\frac{\partial C_i(r,t)}{\partial t} = \nabla \cdot (D_i \nabla C_i(r,t) + z_i \mu_i F C_i(r,t) \nabla V(r,t) + \mu_i C_i(r,t) D_{v_i} \nabla P(r,t)) \quad (4)$$

where D_i is the diffusion coefficient, z_i is the charge number, μ_i is the mobility, D_{v_i} is the molar volume of species i, and F denotes the Faraday constant.

The total ionic current density can be expressed as in Equation (5)

$$J_{\text{tot}}(r,t) = \sum_{i=1}^{N} z_i F f_i(r,t) \quad (5)$$

where the general form of the Nernst–Planck equation for the total flux $\boldsymbol{f_i}$ of an ion species i in Equation (6) consists of three distinct components: diffusion, electromigration, and advection

$$f_i(r,t) = -D_i \nabla C_i(r,t) - z_i \mu_i F C_i(r,t) \nabla V(r,t) - \mu_i C_i(r,t) D_{v_i} \nabla P \quad (6)$$

$$J_{i_{\text{Diff}}}(r,t) = z_i F J_{i_{\text{Diff}}}(r,t) = z_i F D_i \nabla C_i(r,t) \quad (7)$$

This term represents the ion current density due to concentration gradients, driving the species from regions of high concentration to low concentration.

$$J_{i_{\text{EM}}}(r,t) = z_i F f_{i_{\text{EM}}}(r,t) = z_i^2 \mu_i F^2 C_i(r,t) \nabla V(r,t) \quad (8)$$

This term represents the ion current density due to the electric potential gradient ∇V, and is proportional to μ_i, the ion's mobility, and to the factor z_iF representing the electric charge of the species in terms of Faraday's constant.

$$J_{i_{\text{Ad}}}(r,t) = z_i F f_{i_{\text{Ad}}}(r,t) = z_i F \mu_i C_i D_{v_i} \nabla P(r,t) \quad (9)$$

This term represents the transport of mass by the bulk motion of a fluid. The pressure gradient ∇P drives the species contained in the IL in response to an external pressure field, which in this case is the polymer pressure p due to deformation as in Equation (3).

3.3. Electrical Model

The potential distribution (V) inside the BC is calculated in the electrical model solution by using the Poisson equation as reported in the following

$$-\varepsilon_0 \varepsilon_r \nabla^2 V(r,t) = \rho_0 + \sum_{i=1}^{N} z_i e C_i(r,t) \quad (10)$$

where ε_0 is the absolute dielectric constant, ε_r is the relative dielectric constant, ρ_0 is the permanent charge density. The ion concentrations C_i are the coupling factors to the chemical model introduced in Equation (4).

Within the PEDOT domain, the electric potential was assumed to be governed by Ohm law and the current continuity equation, which was implemented separately. In the present formulation, the BC/PEDOT:PSS interface is modeled as an ideal contact following a macroscopic homogenized approach, consistent with prior literature.[9,12,14,36] However, it is worth noting that under large deformation, PEDOT:PSS films may develop microcracks, as reported in the literature,[42,43] which can locally increase resistivity. These nonideal effects, while not currently included in the present framework, could be incorporated in future model refinements through a field-dependent formulation of resistivity.

4. Results

4.1. FEM Model Implementation and Parameters

The model is implemented by FEM simulations in Comsol Multiphysics®,[44] which solve partial differential equations over both spatial and temporal domains and allow coupling between the physical domains.

4.1.1. Mechanical Model

The mechanical deformation of the BC-based sensor was simulated using a 2D FEM model in the xy-plane representing the cantilever configuration of the device (**Figure 3**). The clamped region (Ω_C^{2D}) was fixed with a zero displacement, while a prescribed sinusoidal displacement in the vertical direction was applied to the free tip. The sinusoidal excitation mimics the mechanical input used in the experimental characterization and allows a controlled analysis of the deformation-induced electrochemical phenomena. The model geometry was discretized with a physics-controlled quadrilateral mesh, with a minimum element size of 3 μm and a maximum element size of 800 μm. This provides sufficient resolution near regions with strong curvature and high strain gradient, such as the clamping zone, while ensuring the efficiency of the calculation in less critical regions. The FEM analysis was performed using a linear-elastic formulation where the displacement field was solved as in Section 3.1, from which field variables such as strain, stress, and derived polymer pressure p were calculated as in Equation (2). The polymer pressure value of the mechanical model was extracted along selected cut lines (CL) in the y-direction at 0.1 mm, 0.5 cm, 1 cm, 1.5 cm, and 2 cm from the fixed bracket edge (L_C). It serves as a coupling variable for the mechanoelectric model as in Equation (3).

4.1.2. Chemical and Electrical Model

The ionic transport and the distribution of the electric potential within the BC layer were modeled using a 1D FEM formulation along the y-axis cutlines, orthogonal to the plane of mechanical deformation. The model considers two mobile ionic species, a cation and an anion, via the Nernst–Planck equation as in Equation (4). The local net charge density, defined as the difference between the cation and anion concentrations weighted by their respective charges, served as the source term for the Poisson equation (10), which was solved to obtain the electric potential distribution and calculate the voltage at the electrode terminals for each cutline along the y-axis (Figure 3). For simplicity, each cutline model is treated independently, neglecting lateral coupling effects and the influence of the PEDOT electrode

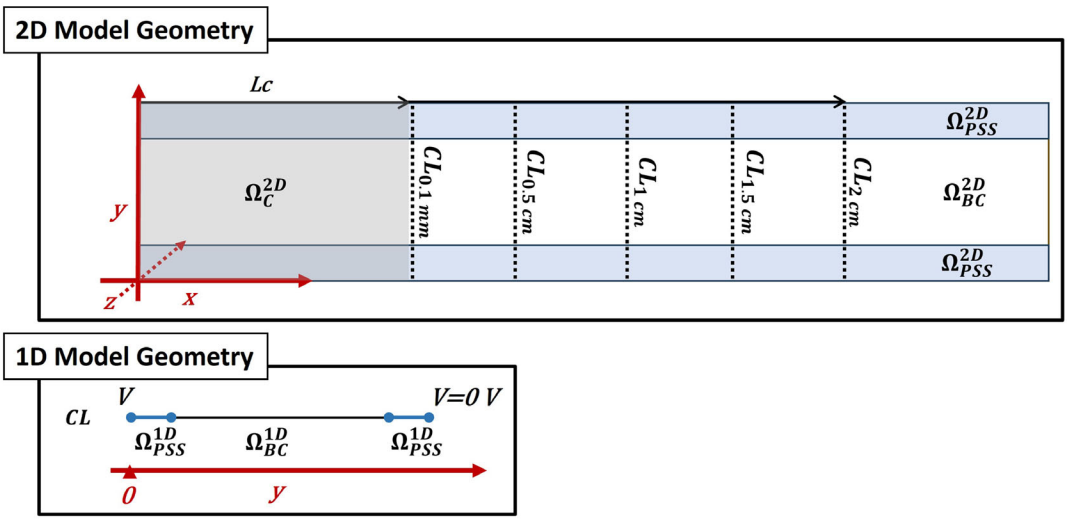

Figure 3. FEM Model Geometry: 2D geometry for the mechanical domain model, and 1D geometry for the mechano-electrical transduction model at the different *y*-axis cutlines.

along the *x*-axis within the 1D domain. At the outer ends of the BC domain (Ω_{BC}^{1D}), zero-flux Neumann boundary conditions were applied to represent ion confinement in the material. Dirichlet boundary conditions were introduced at the interfaces between the BC (Ω_{BC}^{1D}) and the PEDOT:PSS electrodes (Ω_{PSS}^{1D}) to ensure continuity of electric potential at the interfaces. A Dirichlet boundary condition that sets the electric potential to zero ($V = 0$ V) was applied to the outer boundary of the upper electrode to define the electrical ground reference.

4.1.3. Simulation Parameters

The model parameters are determined by experiments or from the literature. When necessary, scaling factors were determined through calibration by comparing the macroscopic model outputs with experimentally measurable field quantities at the selected excitation frequency. Since the model was calibrated under a specific frequency condition, its application to different excitation frequencies may require recalibration to ensure modeling accuracy. **Table 2** contains the parameters associated with the mechanical model. **Table 3** focuses on the electrochemical model and the ionic species, and **Table 4** summarizes the parameters related to the electrical response of the sensor. The Young modulus of the BC–IL–PEDOT sample (E) was determined by dynamic mechanical analysis (DMA) using a 2000 TA DMA produced by Triton Technology Ltd (London, UK). The membrane modulus was determined by applying a sinusoidal force at a frequency of 10 Hz at a working temperature of ≈25 °C to a rectangular sample in single-cantilever mode. Calibration was performed before each measurement using the automatic procedure in the control software of the device. The initial ion concentration C_0 was calculated based on the amount of IL present in the sample, and the number of moles was determined by dividing this value by the molecular weight of the IL.

Table 2. Mechanical parameters.

Parameter description	Value	Unit
Young modulus of BC–IL–PEDOT compound, E	1.64	GPa
Poisson ratio of BC, ν_{BC}[45]	0.01	–
Poisson ratio of PEDOT, ν_{PSS}[46]	0.435	–
Mass density of BC, ρ_{BC}	0.904	g cm^{-3}
Mass density of PEDOT, ρ_{PSS}[47]	1.28	g cm^{-3}

Table 3. Chemical parameters.

Parameter description	Value	Unit
Initial ion concentration, C_0 (EMIM-BF_4)	740.88	mol m^{-3}
Cation diffusion constant,[48] D_{cat}	4×10^{-10}	m^2 s^{-1}
Anion diffusion constant,[48] D_{an} (BF_4)	4.4×10^{-10}	m^2 s^{-1}
Cation molar volume,[49] $D_{\nu_{cat}}$	1.15×10^{-4}	m^3 mol^{-1}
Anion molar volume,[49] $D_{\nu_{an}}$ (BF_4)	3.85×10^{-5}	m^3 mol^{-1}
Cation charge number, Z_{cat}	1	–
Anion charge number, Z_{an}	−1	–
Universal gas constant, R	8.31	J (K · mol)$^{-1}$
Temperature, T	298.15	K
Cation mobility, μ_{cat}	$D_{cat}/(R \cdot T)$	s · mol kg^{-1}
Anion mobility, μ_{an}	$D_{an}/(R \cdot T)$	s · mol kg^{-1}

Table 4. Electrical parameters.

Parameter description	Value	Unit
Electrical conductivity of PEDOT, σ_{PSS}[50]	10	S m^{-1}
Effective absolute dielectric permittivity of BC–IL–PEDOT compound, $\varepsilon = \varepsilon_r\varepsilon_0$	Calibrated (Figure 6)	F m^{-1}

The resulting value was converted to moles per cubic meters taking into account the sample volume.

4.2. Experimental and FEM-Based Analysis

In this section, a combined experimental and numerical investigation of the BC–IL sensor under dynamic loading is presented. First, experimental measurements are discussed and then compared with simulations performed with a multiphysics FEM framework. The analysis is divided into subsections dealing with experimental data acquisition and model results, including 2D mechanical response, 1D mechanoelectrical model calibration, and ionic current density evaluation on selected y-axis cutlines.

4.2.1. Experimental Acquisition

The mechanoelectrical properties of the BC-based composites were evaluated by mounting the samples in a cantilever configuration. In this setup, the free end of the cantilevered transducer was subjected to controlled mechanical excitation. **Figure 4** shows the acquisition of an imposed sinusoidal tip motion at a selected frequency of 8 Hz with a peak amplitude of $d_{MAX} = 0.27$ mm, measured using a laser detector. The voltage response of the sensor shows a periodic signal with a peak amplitude of $V_p = 0.14$ mV, which determines an experimental ratio of $0.52\ \mathrm{V\,m^{-1}}$ (corresponding to an attenuation of $A_{exp} = -6$ dB) and a phase delay of $\Phi_{exp} = -30.7°$.

4.2.2. Mechanical Model

A 2D FEM simulation was performed in the xy-plane by applying a sinusoidal displacement at the cantilever tip, with a frequency of 8 Hz and a peak amplitude of $d_{MAX} = 0.27$ mm. This displacement matches the experimental measurement shown in Figure 4 and obtained using the setup detailed in the Section 2.2.

The solution of the 2D mechanical model in terms of polymer pressure (p) is shown in **Figure 5**. The pressure distribution shows higher values in regions with maximum curvature and near the electrode boundaries. The pressure values were extracted along five selected y-axis cutlines ($CL_{0.1\,mm}$, $CL_{0.5\,cm}$, $CL_{1\,cm}$, $CL_{1.5\,cm}$, $CL_{2\,cm}$) considered at different distances from the fixed clamp and detailed in Figure 3 of the Methods Section 4.2.

4.2.3. Dual-Carrier Mecchano-Electrical Model Calibration

Effective absolute dielectric permittivity ε of the compound material plays a critical role in determining the amplitude and phase characteristics of the response of the BC–IL sensor. This dependance results from the influence of ε on the capacitive behavior of the system, which determines the dynamics of charge redistribution during mechanical deformation.

A 1D FEM model was employed along the y-axis cutlines, perpendicular to the mechanical deformation plane, to simulate ion migration and the associated electric potential distribution across the BC layer (details in Section 4.2). The calibration of the permittivity of the BC sensor ε was performed by a parametric analysis of the model response for the cutline $CL_{0.1\,mm}$ configuration by minimizing the cost function determined as the sum of the normalized root mean square errors (RMSEs) of the simulation results with respect to the experimentally observed amplitute ratio A_{exp} and phase shift Φ_{exp} for a sinusoidal input at 8 Hz. The search space for permittivity was defined based on literature values reported for similar systems, including sensors made of graphene and chitosan with the IL EMIM-BF_4, which have a permittivity of $2.8 \times 10^{-2}\ \mathrm{F\,m^{-1}}$,[12] and IPMCs based on water-hydrated Nafion, whose permittivity is between 5×10^{-2} and $6 \times 10^{-1}\ \mathrm{F\,m^{-1}}$.[9] **Figure 6** illustrates the trend of the total RMSE, calculated as the sum of the normalized RMSEs for attenuation and phase shift, and highlights the optimal permittivity value $\varepsilon = 2.24 \times 10^{-2}\ \mathrm{F\,m^{-1}}$, which minimizes the cost function.

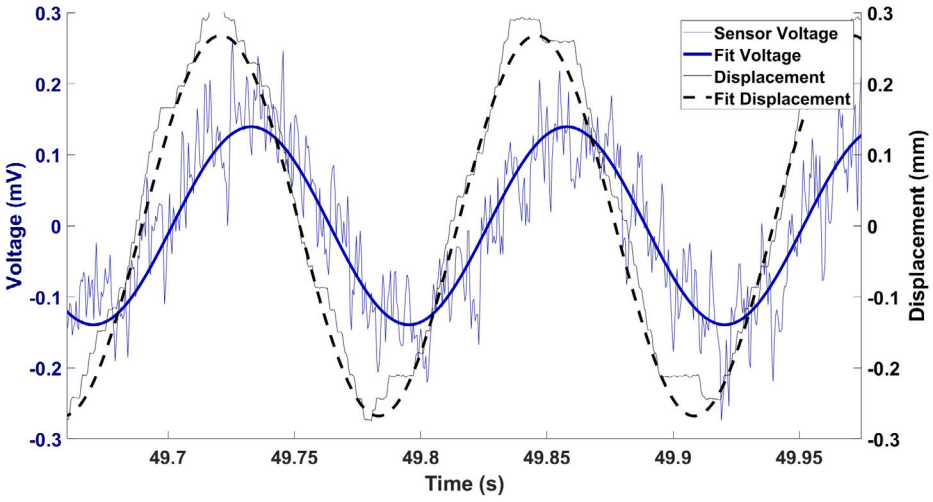

Figure 4. Experimental response of the BC sensor infused with EMIM-BF_4 to sinusoidal input displacements with amplitude $d_{MAX} = 0.27$ mm and frequency $f_d = 8$ Hz. The recorded signals were fitted using single-frequency sinusoids to filter noise and accurately extract amplitude and phase shift parameters.

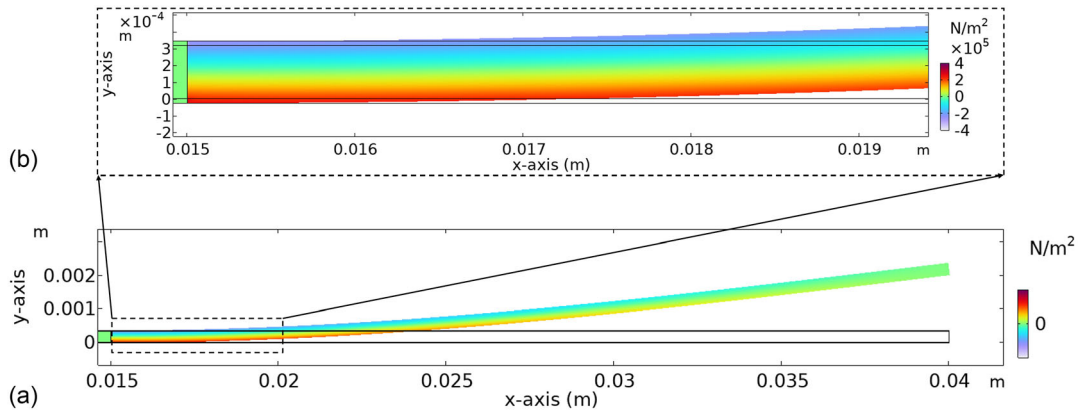

Figure 5. Pressure field distribution in the polymer domain a) computed from the 2D mechanical model at the time of maximum applied displacement, including in b) a zoomed-in view of the area exhibiting the highest pressure values and spatial gradient.

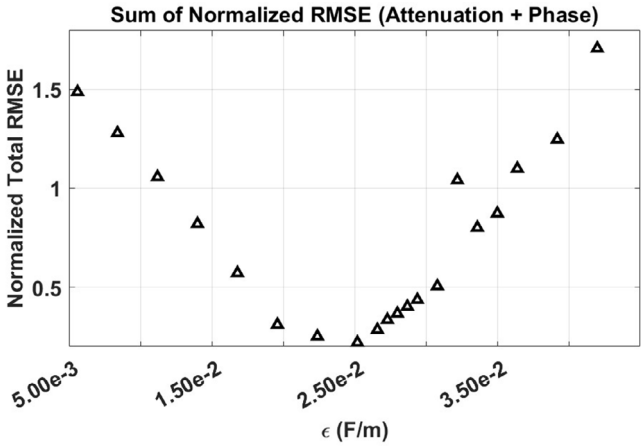

Figure 6. Calibration curve for the BC-sensor permittivity ϵ. The plot shows the sum of the normalized RMSEs for the attenuation and phase shift between the sensor voltage and the tip displacement, computed with respect to the experimental reference values A_{exp} and phase shift Φ_{exp} for a sinusoidal input at 8 Hz.

The value determined is within 10% of the chitosan-based ref. [12] and thus confirms its agreement with comparable material systems. This optimum setting corresponds to discrepancies with respect to experimental values of $3.4 \times 10^{-2}\,\mathrm{V\,m^{-1}}$ for the amplitude ratio A and 1.6° for the phase Φ. The close agreement between simulations and experimental results, in both amplitude and phase, together with the stability observed across repeated measurements,[40,41] indicates that the electrode/active-layer interface quality did not significantly affect the device response under the tested conditions.

4.2.4. Position-Dependent Sensor Response and Curvature Effects

Figure 7a illustrates the simulated response of the sensor voltage evaluated along the five selected y-axis cutline models. The results show a clear dependance of the electrical response of the composite in accordance with the position along the beam, which correlates with the spatial distribution of the mechanical stress and pressure gradient in Figure 5. In particular, the cutline closest to the fixed clamp ($CL_{0.1\,mm}$) shows the highest amplitude response, which agrees with the proposed transduction mechanism. This region corresponds to the section of maximum curvature of the cantilever. This increased curvature leads to a higher pressure gradient in the y direction, which directly affects the advection term in the Nernst–Planck equation and triggers ionic movement and charge separation. At larger distances from the clamp, both the pressure and its spatial gradient decrease due to the lower curvature, resulting in a smaller electrical response. These results emphasize the importance of local deformation and stress distribution in shaping the overall sensor response. In particular, large deformations near the clamp region can induce sideways microcracks in soft material electrodes, as reported in previous studies,[42,43] leading to increased local resistivity. As a result, the highly deformed zones near the clamp can be electrically decoupled from the rest of the sensor, maintaining a localized electrical response. This observation supports the assumption of neglecting the influence of the PEDOT electrodes in the transverse (x) direction.

4.2.5. Ionic Current Densities

The behavior of ionic transport was analyzed by examining the temporal evolution of the total ionic current density as in Equation (5) and its components, diffusion, electromigration, and advection, at specific time instants of both the input displacement cycle and the resulting sensor voltage response. In Figure 7b,c broken y-axis is used to highlight interfacial effects, as the current densities remain nearly constant in the inner region of the BC. The first analysis reveals the dynamic interplay between mechanically induced pressure gradients and ionic transport. It highlights how advection dominates during displacement extrema, while electromigration becomes prominent when the displacement velocity approaches zero. Figure 7b, corresponding to the maximum displacement, shows that advection is the dominant component due to the fluid motion induced by the structural deformation. In contrast, the diffusion and electromigration currents counteract the advection as they are driven by

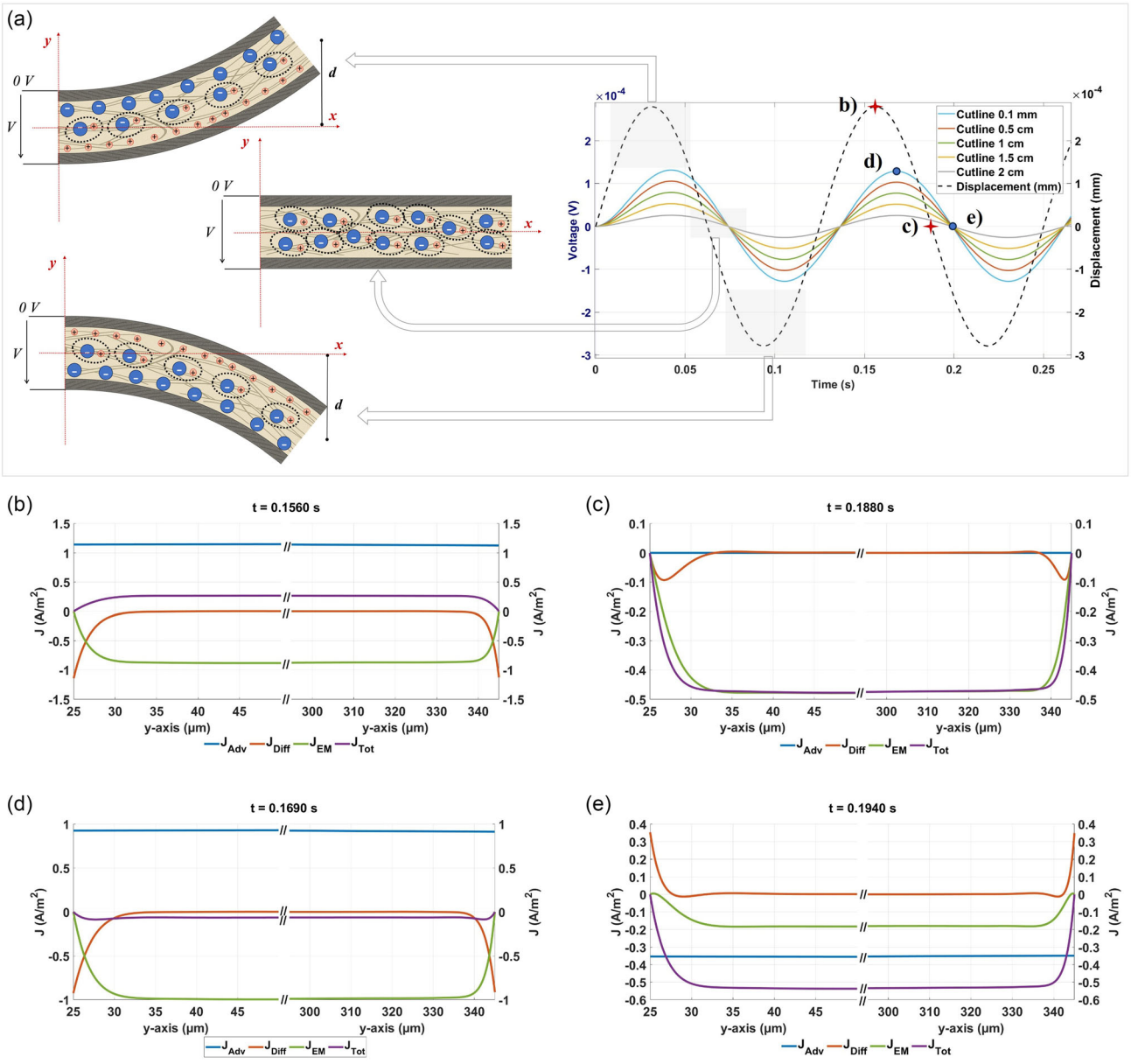

Figure 7. Simulation results for the BC–IL sensor under dynamic excitation. a) Simulated voltage responses at various positions along the beam length, $CL_{0.1\ mm}$, $CL_{0.5\ cm}$, $CL_{1\ cm}$, and $CL_{2\ cm}$, illustrating the spatial dependance of the electrical output. The panel also includes a schematic illustration of the dual-ion sensing mechanism, highlighting the redistribution of cations and anions at positive displacement, negative displacement, and close to zero displacement. b,c) Spatial profile on the *y*-axis $CL_{0.1\ mm}$ cutline of the total ionic current density and its components (diffusion, electromigration, and advection) at key points of the displacement cycle: (b) maximum displacement and (c) zero displacement during the falling edge. d,e) Spatial profile on the *y*-axis $CL_{0.1\ mm}$ cutline of the ionic current density at characteristic points of the sensor voltage waveform: d) voltage peak and e) zero voltage during the falling edge.

residual electric fields from the previous moments and local concentration gradients. In Figure 7c, which shows the falling edge at zero displacement, the advection component disappears as the instantaneous velocity is zero. Under these conditions, electromigration becomes the dominant component of the total current, driven by the electric field resulting from the previous charge displacements. The diffusion current generally remains weak, but shows localized significance at the BC/PEDOT interface, while it is negligible in the bulk region. Overall, the diffusion and electromigration components are largely in phase, while the advection current is out of phase with them, yet still plays a crucial role as the primary initiator of the sensing mechanism. The phase delay between these three transport phenomena is responsible for the resulting phase shift between the measured sensor voltage and the mechanical excitation. The ionic current density distribution corresponding to the minimum displacement shows dynamics analogous to Figure 7b, but with the advection direction reversed. The current density corresponding

to the zero displacement during the rising edge matches the conditions of Figure 7c, where advection is negligible and electromigration dominates near the interface. The second analysis, which is based on characteristic points of the sensor voltage, provides valuable insights into the electrochemical dynamics underlying the generation of the electrical signal. It illustrates how the phase shift between the ionic motion and the mechanical excitation contributes to the observed response of the sensor voltage. Together with the displacement-based analysis, these complementary perspectives provide a comprehensive understanding of the spatio-temporal coupling mechanisms governing mechanoelectric transduction in BC–IL sensors. In Figure 7d, which corresponds to the voltage peak, the net ionic current can be assumed to be zero. A slightly negative value is reported due to the impossibility of identifying the exact instant of the peak. At this point, the three components of the ionic current, advection, electromigration and diffusion, are approximately balanced. This configuration corresponds to the out-of-phase equilibrium between the mechanical input and the electrical output. In Figure 7e, the current density becomes clearly negative, which is consistent with the sensor reaching the maximum negative slope of the voltage waveform.

This detailed analysis offers a comprehensive understanding of the sensing mechanism and provides design guidelines for IL selection tailored to application-specific requirements such as response speed and phase behavior. The investigation of the components of the ionic current at critical displacement and voltage instants reveals the complex interplay of advection, electromigration, and diffusion, and their collective influence on charge redistribution. In particular, the phase lag between mechanical deformation and ionic movement is identified as a key factor for the voltage response. Furthermore, the localized contribution of the diffusion current at the BC-PEDOT interface underlines the importance of interfacial phenomena for the overall electromechanical behavior of the sensor.

5. Conclusions

This work presents, for the first time, a first-principle white-box FEM for the characterization of dual-ion EAP sensors based on BC and ILs. BC is a low-cost, green, and fully biodegradable material that offers significant environmental advantages over synthetic or plant-derived alternatives, particularly in the context of sustainable electronics. It can be produced through bacterial fermentation using green feeding sources, including organic waste such as banana peels, further reducing its environmental impact and making its production process both sustainable and circular. Unlike conventional materials previously employed for similar applications, BC–IL composites require a dual-carrier ionic transport model, an aspect never addressed in the literature until now. By combining a 2D FEM mechanical model with a series of 1D electrochemical sub-models, we have developed a computationally efficient yet physically grounded framework suitable for rapid prototyping. The model accurately represents the mechanoelectrical transduction process through the coupling of pressure-induced ionic transport and potential generation and has been quantitatively validated using experimental data. The analysis shows that the sensor response is predominantly determined by the regions of highest curvature near the fixed clamp, where pressure gradients and advection effects are maximized. The dimensional decomposition significantly reduces computational cost while preserving essential physical behavior, enabling rapid exploration of material and geometric parameters.

This study validates the framework on BC–IL composites, yet the formulation is general and material-independent. The coupled mechanical and electrochemical domains are governed by fundamental continuum and transport equations, and require only the substitution of material-specific parameters (elastic modulus, dielectric constant, ion diffusivity, etc.) to be applied to any porous, ionic-liquid-infused polymer matrix, including Nafion, chitosan, graphene-based systems, or other ionomeric materials. The introduction of a dual-ion transport framework represents the key novelty of this work, moving beyond single-carrier models and enabling accurate prediction of coupled ionic dynamics and charge generation. The proposed approach, therefore, constitutes a versatile and extensible design tool, suitable for a broad class of smart and environmentally responsible polymeric systems.

Therefore, this modeling strategy establishes a scalable platform for the development and optimization of next-generation green sensors. Future work will extend the model to a broader range of excitation frequencies, IL chemistries, and electrode configurations, and will incorporate field-dependent parameters to capture non-idealities at the electrode/active-layer interface, thereby further broadening its applicability in sustainable electronic systems.

Acknowledgements

This work was funded by European Union—Next Generation EU, Missione 4 Componente 1 CUP J53D23003460006 Green sensing systems based on Bacterial Cellulose (SENS-BC).

Open access publishing facilitated by Universita degli Studi di Messina, as part of the Wiley - CRUI-CARE agreement.

Conflict of Interest

The authors declare no conflict of interest.

Author Contributions

Francesca Sapuppo: conceptualization (equal); data curation (lead); formal analysis (lead); investigation (equal); methodology (equal); software (lead); validation (equal); visualization (lead); writing—original draft (lead). **Giovanna Di Pasquale**: investigation (supporting); writing—review & editing (supporting). **Salvatore Graziani**: conceptualization (equal); formal analysis (equal); funding acquisition (equal); investigation (supporting); methodology (equal); project administration (equal); resources (equal); writing—review & editing (equal). **Sara Sadat Hosseini**: investigation (supporting). **Luca Patanè**: conceptualization (equal); methodology (equal); project administration (supporting); resources (supporting); validation (supporting); writing—review & editing (equal). **Antonino Pollicino**: investigation (supporting); resources (equal); writing—review & editing (supporting). **Carlo Trigona**: resources (equal); validation (equal). **Maria Gabriella Xibilia**: conceptualization (equal); methodology (equal); project administration (equal); resources (equal); writing—review & editing (equal).

Data Availability Statement

The data that support the findings of this study are available from the corresponding author upon reasonable request.

Keywords

bacterial cellulose, computational modeling, finite element method, multiphysics, organic sensors, smart materials

Received: May 28, 2025
Revised: August 29, 2025
Published online:

[1] T. Wang, M. Farajollahi, Y. S. Choi, et al., "Electroactive polymers for sensing," *Interface Focus 6*, no. 4 (**2016**): 20160026.
[2] S. W. Park, S. J. Kim, S. H. Park, J. Lee, H. Kim, and M. K. Kim, "Recent Progress in Development and Applications of Ionic Polymer-Metal Composite," *Micromachines 13* (**2022**): 8.
[3] Q. He, D. Vokoun, T. Stalbaum, et al., "Mechanoelectric transduction of ionic polymer-graphene composite sensor with ionic liquid as electrolyte," *Sensors and Actuators A: Physical 286* (**2019**): 68.
[4] J. Jiang, C. Lin, S. Xu, Y. Yu, L. Yao, and Z. Huang, "Application-oriented modeling of soft actuator ionic polymer–metal composites: a review," *Advanced Intelligent Systems 6* (**2023**): 3.
[5] N. El-Atab, R. B. Mishra, F. Al-Modaf, et al., "Soft actuators for soft robotic applications: a review," *Advanced Intelligent Systems 2*, no. 10 (**2020**): 2000128.
[6] A. Sarker, T. Ul Islam, and M. R. Islam, "A review on recent trends of bioinspired soft robotics: actuators, control methods, materials selection, sensors, challenges, and future prospects," *Advanced Intelligent Systems 7* (**2024**): 3.
[7] H. Cui, Q. Zhao, L. Zhang, and X. Du, "Intelligent polymer-based bioinspired actuators: from monofunction to multifunction," *Advanced Intelligent Systems 2* (**2020**): 11.
[8] S. Nemat-Nasser and J. Li, "Electromechanical response of ionic polymer-metal composites," *Journal of Applied Physics 87* (**2000**): 3321.
[9] D. Pugal, *Physics Based Model of Ionic Polymer-Metal Composite Electromechanical and Mechanoelectrical Transduction* (University of Nevada, **2012**).
[10] K. M. Newbury, "*Characterization, Modeling, and Control of Ionic Polymer Transducers*" (Ph.D. thesis, Virginia Polytechnic Institute and State University, **2002**).
[11] K. Newbury and D. Leo, "Electromechanical Modeling and characterization of ionic polymer benders" *Journal of Intelligent Material Systems and Structures 13* (**2002**): 51.
[12] Q. He, D. Vokoun, T. Stalbaum, et al., "Mechanoelectric transduction of ionic polymer-graphene composite sensor with ionic liquid as electrolyte," *Sensors and Actuators A: Physical 286* (**2019**): 68.
[13] L. Patanè, F. Sapuppo, M. Calapristi, et al., "A multiphysics Framework for Bacterial Cellulose Sensor Modeling," in *2024 IEEE International Conference on Metrology for eXtended Reality, Artificial Intelligence and Neural Engineering* (IEEE, **2024**).
[14] D. Pugal, P. Solin, A. Aabloo, and K. J. Kim, "IPMC mechanoelectrical transduction: its scalability and optimization," *Smart Materials and Structures 22*, no. 6 (**2013**): 125029.
[15] L. Yang, Y. Yang, and H. Wang, "Modeling and control of ionic polymer metal composite actuators: a review," *European Polymer Journal 186* (**2023**): 111821.
[16] E. K. Sijabat, A. Nuruddin, P. Aditiawati, and B. Sunendar Purwasasmita, "Optimization on the synthesis of bacterial nano cellulose (BNC) from banana peel waste for water filter membrane applications," *Materials Research Express 7*, no. 5 (**2020**): 055010.
[17] F. Esa, S. Tasirin, and N. Abd Rahman, "Overview of bacterial cellulose production and application," *Agriculture and Agricultural Science Procedia 2* (**2014**): 113.
[18] J. Huang, M. Zhao, Y. Hao, and Q. Wei, "Recent advances in functional bacterial cellulose for wearable physical sensing applications," *Advanced Materials Technologies 7*, no. 1 (**2022**): 2100617.
[19] J. D. Yuen, L. C. Shriver-Lake, S. A. Walper, D. Zabetakis, J. C. Breger, and D. A. Stenger, "Microbial nanocellulose printed circuit boards for medical sensing," *Sensors 20* (**2020**): 7.
[20] G. D. Pasquale, S. Graziani, A. Pollicino, and C. Trigona, "A Bacterial Cellulose Based Mass Sensor" in *2019 IEEE International Symposium on Measurements and Networking (M and N)* (IEEE, **2019**), 1–4.
[21] C. Trigona, S. Cerruto, S. Graziani, G. Di Pasquale, and A. Pollicino, "Towards environmentally friendly accelerometers based on bacterial cellulose," *Applied Sciences 11* (**2021**): 17.
[22] J. Wang, J. Tavakoli, and Y. Tang, "Bacterial cellulose production, properties and applications with different culture methods—a review," *Carbohydrate Polymers 219* (**2019**): 63.
[23] G. D. Pasquale, S. Graziani, A. Pollicino, and C. Trigona, "Performance characterization of a biodegradable deformation sensor based on bacterial cellulose," *IEEE Transactions on Instrumentation and Measurement 69*, no. 5 (**2020**): 2561.
[24] G. D. Pasquale, S. Graziani, A. Licciulli, R. Nisi, A. Pollicino, and C. Trigona, "Geometrical Analysis of a Bacterial Cellulose-Based Sensing Element," in *Proceedings of the IEEE International Instrumentation and Measurement Technology Conference (I2MTC)* (IEEE, **2019**), 225–228.
[25] B. Kanjilal, Y. Zhu, V. Krishnadoss, et al., "Bioionic liquids: enabling a paradigm shift toward advanced and smart biomedical applications", *Advanced Intelligent Systems 5* (**2023**): 5.
[26] R. Caponetto, S. Graziani, F. Sapuppo, and V. Tomasello, "An enhanced fractional order model of ionic polymer–metal composites actuator," *Advances in Mathematical Physics 2013* (**2013**): 1.
[27] R. Caponetto, S. Graziani, F. Pappalardo, and F. Sapuppo, "Identification of IPMC nonlinear model via single and multi-objective optimization algorithms," *ISA Transactions 53*, no. 2 (**2014**): 481.
[28] M. Vahabi, E. Mehdizadeh, M. Kabganian, and F. Barazandeh, "Experimental identification of IPMC actuator parameters through incorporation of linear and nonlinear least squares methods," *Sensors and Actuators A: Physical 168*, no. 1 (**2011**) 140.
[29] A. Punning, U. Johanson, M. Anton, A. Aabloo, and M. Kruusmaa, "A distributed model of ionomeric polymer metal composite," *Journal of Intelligent Material Systems and Structures*, *20*, no. 14 (**2009**): 1711.
[30] R. Caponetto, V. De Luca, S. Graziani, F. Sapuppo, and G. Di Pasquale, "IPMC Frequency Dependent Multiphysics Model Considering Electrodes High Surface and Fractional Effects," in *2014 IEEE International Instrumentation and Measurement Technology Conference (I2MTC) Proceedings* (IEEE, **2014**), 1529–1532.
[31] R. M. Auenhammer, J. Kim, C. Oddy, et al., "X-ray scattering tensor tomography based finite element modelling of heterogeneous materials," *npj Computational Materials 10* (**2024**): 1.
[32] W. Li and X. S. Zhang, "Computational morphogenesis for liquid crystal elastomer metamaterial," *npj Computational Materials 10* (**2024**): 1.
[33] M. A. Moreno-Mateos, M. Hossain, P. Steinmann, and D. Garcia-Gonzalez, "Hybrid magnetorheological elastomers enable versatile soft actuators," *npj Computational Materials 8* (**2022**): 1.
[34] R. Caponetto, V. De Luca, G. Di Pasquale, S. Graziani, F. Sapuppo, and E. Umana, "A multiphysics frequency-dependent model of an

IP^{2}C actuator," *IEEE Transactions on Instrumentation and Measurement 63*, no. 5 (**2014**): 1347.
[35] R. Caponetto, V. D. Luca, S. Graziani, and F. Sapuppo, "An optimized frequency-dependent multiphysics model for an ionic polymer metal composite actuator with ethylene glycol as the solvent," *Smart Materials and Structures 22*, no. 12 (**2013**): 125016.
[36] D. Pugal, K. Jung, A. Aabloo, and K. Kim, "Ionic polymer-metal composite mechanoelectrical transduction: review and perspectives," *Polymer International 59* (**2010**): 279.
[37] R. Caponetto, G. Di Pasquale, S. Graziani, A. Pollicino, F. Sapuppo, and C. Trigona, "Modeling of bacterial cellulose-based composite," *Electronics 12* (**2023**): 21.
[38] A. Aabloo, G. Di Pasquale, S. Graziani, et al., "A Green Deformation Sensor Based on Bacterial Cellulose and Bio-Derived Ionic Liquids," in *2021 18th International Multi-Conference on Systems, Signals and Devices (SSD)* (IEEE, **2021**), 1182–1185.
[39] T. Khan, G. Vadivel, B. Ramasamy, G. Murugesan, and T. A. Sebaey, "Biodegradable conducting polymer-based composites for biomedical applications—a review," *Polymers 16* (**2024**): 11.
[40] G. Di Pasquale, S. Graziani, S. S. Hosseini, et al., "Frequency Investigation of Bio-Polymer Based Motion Sensors," in *2025 IEEE Sensors Applications Symposium (SAS)* (IEEE, **2025**), 1–5.
[41] G. Di Pasquale, S. Graziani, S. S. Hosseini, et al., "Frequency Investigation of Open-Circuit and Short-Circuit Signals Produced by a Bio-Polymer Based Deformation Sensor," in *2025 IEEE Medical Measurements and Applications (MeMeA)* (IEEE, **2025**), 1–6.
[42] X. Zhang, W. Yang, H. Zhang, M. Xie, and X. Duan, "PEDOT:PSS: From conductive polymers to sensors," *Nanotechnology and Precision Engineering 4*, no. 4 (**2021**): 045004.
[43] M. A. Moreno-Mateos and P. Steinmann, "Crosslinking degree variations enable programming and controlling soft fracture via sideways cracking," *npj Computational Materials 10* (**2024**): 1.
[44] COMSOL Multiphysics®, www.comsol.com, (accessed: January 2024).
[45] P. Lopez-Sanchez, M. Rincon, D. Wang, S. Brulhart, J. R. Stokes, and M. J. Gidley, "Micromechanics and poroelasticity of hydrated cellulose networks" *Biomacromolecules 15*, no. 6 (**2014**): 2274, pMID: 24784575.
[46] R. Agbaoye, P. Adebambo, J. Akinlami, et al., "Elastic constants and mechanical properties of PEDOT from first principles calculations," *Computational Materials Science 139* (**2017**): 234.
[47] X. Crispin, F. L. E. Jakobsson, A. Crispin, et al., "*The origin of the high conductivity of poly(3,4-ethylenedioxythiophene)-poly(styrenesulfonate) (PEDOT-PSS)*," *Chemistry of Materials 18*, no. 18 (**2006**): 4354.
[48] K. Hayamizu, Y. Aihara, H. Nakagawa, T. Nukuda, and W. Price, "Ionic conduction and ion diffusion in binary room-temperature ionic liquids composed of [emim][BF4] and LiBF4," *Journal of Physical Chemistry B 108* (**2004**): 19527.
[49] M. G. Montalbán, C. L. Bolívar, F. Guillermo Díaz Baños, and G. Víllora, "Effect of temperature, anion, and alkyl chain length on the density and refractive index of 1-Alkyl-3-methylimidazolium-based ionic liquids," *Journal of Chemical and Engineering Data 60* (**2015**).
[50] J. Ouyang, Q. Xu, C.-W. Chu, Y. Yang, G. Li, and J. Shinar, "On the mechanism of conductivity enhancement in poly(3,4-ethylenedioxythiophene):poly(styrene sulfonate) film through solvent treatment," *Polymer 45*, no. 25 (**2004**): 8443.